MICROSCOPIC ORIGIN OF NONLINEAR OPTICAL PROPERTIES OF

2D MATERIALS: A FIRST PRINCIPLES STUDY

An Undergraduate Research Scholars Thesis

by

ALEX MATTHEW STRASSER

Submitted to the Undergraduate Research Scholars program at
Texas A&M University
in partial fulfillment of the requirements for the designation as an

UNDERGRADUATE RESEARCH SCHOLAR

Approved by Research Advisor: Dr. Xiaofeng Qian

May 2020

Major: Chemical Engineering

TABLE OF CONTENTS

ABSTRACT

Microscopic Origin of Nonlinear Optical Properties of 2D Materials: A First Principles Study

Alex Strasser
Department of Chemical Engineering
Texas A&M University

Research Advisor: Dr. Xiaofeng Qian
Department of Materials Science and Engineering
Texas A&M University

Two-dimensional (2D) transition metal dichalcogenides (TMDCs) have provided a unique materials platform with a variety of interesting optoelectronic properties and great potential for device applications. Janus 2D TMDCs represent a new class of 2D materials whose crystalline symmetry and physical properties can be tailored via Janus structure engineering. Here we present our first-principles study of nonlinear optical properties in Janus 2D TMDCs. Electronic structures such as linear and nonlinear optical properties were calculated using first-principles density functional theory and analyzed in combination with group theory. The microscopic origin of these nonlinear optical properties of Janus TMDCs is elaborated by k-point resolved optical absorption, shift current, and shift vector. We found that the absence of horizontal mirror plane in Janus 2D materials enables the out-of-plane second harmonic generation (SHG) and other nonlinear optical phenomena, such as shift photocurrent and circular photocurrent. Janus 2D materials, therefore, offer a unique platform for exploring nonlinear optical phenomena and designing configurable layered nonlinear optical materials.

ACKNOWLEDGMENTS

NOMENCLATURE

DFT   Density Functional Theory

NLO   Nonlinear Optics/Nonlinear Optical

2D   Two-dimensional

TMDCs   Transition metal dichalcogenides

SHG   Second harmonic generation

VESTA   Visualization for Electronic and Structural Analysis

CHAPTER I

INTRODUCTION

2D Materials

Ever since the discovery of graphene in 2004,[1] two-dimensional (2D) materials have been an important area of research owing to their potential applications in electronics, optics, and many other functional devices. To date, graphene, transition metal dichalcogenides (TMDCs), and hexagonal boron nitride have been extensively studied, exhibiting semimetal, semiconductor, and insulator, respectively. However, there is a great need to explore 2D materials beyond these well-known materials family and beyond the conventional electronic and optical properties.

Janus 2D Materials

Nonlinear optical properties of 2D materials represent a rich class of physical properties that are not only important for fundamental science, but also of high interest to advanced technological applications.[2] In parallel, Janus 2D materials are also a rising area that engineer conventional TMDCs into Janus structure with distinct symmetry, chemical composition, and physical and chemical properties. Janus 2D materials have been explored in the recent studies[3–8] such as HfSSe,[9] WSSe,[10–12] other Janus structures,[13–15] TMDCs based on vanadium,[16] platinum,[17] or yttrium, heterostructures containing Janus 2D materials,[18–26] and a high-throughput theoretical prediction of novel Janus 2D materials.[27]

Janus 2D MoSSe was first synthesized in 2017[28,29] using chemical vapor deposition (CVD), one group selenizing MoS_2,[28] and the other group sulfurizing $MoSe_2$.[29] Janus MoSSe is promising for a wide range of applications in valleytronics,[30] water-splitting photocatalysis,[31]

strain-sensing,[32] gas sensing,[32] thermoelectrics,[33] piezoelectricity,[34] and advanced optical devices.[35]

Several studies have been carried out for bilayer Janus MoSSe.[36–39] A variety of heterostructures can be produced using a dry or wet-etch transfer process once monolayers of Janus MoSSe have been synthesized. Alternatively, a bilayer of MoS_2 or $MoSe_2$ can be grown with CVD and then the top layer can be selenized or sulfurized, respectively, to produce the Janus MoSSe structure.

In this thesis, the nonlinear optical properties of Janus MoSSe are explored and reported. In particular, strong second harmonic generation (SHG) and second-order nonlinear photocurrents, including shift and circular photocurrent, are predicted using first-principles theoretical approach. Finally, k-point resolved optical absorption and shift vector plots are shown to demonstrate the microscopic origin of the nonlinear optical properties of Janus MoSSe. The results clearly demonstrate that Janus structure engineering is a facile approach to transform well-studied 2D materials into a new family of 2D materials with distinct symmetry and physical properties and enable unique NLO responses that are absent in their pristine non-Janus form.

CHAPTER II

METHODOLOGY

All the research tasks were carried out using first-principles electronic structure theory and code by solving many-electron Schrödinger equation with density functional theory (DFT).[40,41]

The general workflow is described as follows. First, a file of atomic positions (POSCAR) was downloaded from Materials Project[42] and was subsequently modified from the default bulk (3D) form into its 2D form by deleting one of the monolayers from the two-monolayer unit cell. This information was fed into DFT calculations performed using Vienna ab initio Simulation Package (VASP)[43,44] to relax the crystal structures and obtain the optimized crystal symmetries, electronic band structure, and electric dipole matrix elements. The latter are then fed into an in-house developed package (iNLO). Both linear and nonlinear optical calculations were performed using iNLO and were subsequently benchmarked by comparing the linear optical data between iNLO and VASP. Data was then analyzed using MATLAB, Python with a variety of Python libraries such as Pymatgen[45] and Numpy, and Mathematica. This workflow is summarized in Figure 1. More specific details about the calculations performed in VASP and iNLO are provided next.
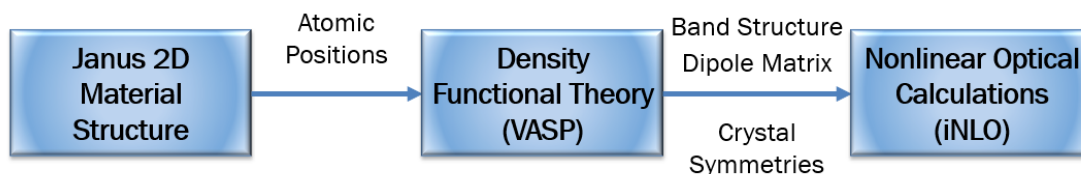

Figure 1: General workflow of information and calculations

DFT Calculations

VASP was used to carry out DFT calculations using the projector-augmented wave (PAW) method,[46,47] generalized gradient approximation in the Perdew-Burke-Ernzerhof form[48] and plane-wave basis with an energy cutoff of 400 eV. The process proceeded in multiple steps. First, a structural relaxation was performed to ensure that the material was relaxed to its minimum energy configuration to ensure local thermodynamic and dynamical stability. This structural relaxation allows the atoms and unit cell to adjust to find their minimum energy configuration. The lattice parameters and bond lengths were compared with experimental values. Then, a static calculation was performed without allowing atomic movements for calculating properties of the material. This information was then fed into both electronic band structure calculations and nonlinear optical calculations in iNLO.

For the structural relaxation, the convergence criteria for atomic force were set to 0.005 eV/Å for the residual maximum force. A vacuum of ~20 Å was added between layers to minimize artificial image interaction between layers due to the periodic boundary condition used in the DFT calculations. During structural relaxation, the z lattice vector was fixed to ensure this vacuum distance was retained. For the initial relaxation and static calculation, the k-point sampling was a 10x10x1 grid. For the nonlinear optical calculations, the k-point sampling was increased to 70x70x1 to ensure the convergence of NLO properties. In general, 80 bands were used for both static and iNLO calculations, which is enough to reach the convergence with respect to number of bands, as the NLO properties were calculated using the sum-over-states approach.

Nonlinear Optical Response Calculations

The in-house package, iNLO, for computing nonlinear optical properties of materials was developed by my advisor, Dr. Xiaofeng Qian, and my mentor, Hua Wang. The calculation starts with a static DFT calculation with additional parameters in the INCAR input file (LOPTICS, LVEL = T) to provide the necessary data for the following NLO calculations. iNLO then uses the data from the above static DFT calculation as input data in conjunction with an iNLO input file for specifying the energy range, energy grid, etc. for the NLO calculation. iNLO also takes advantage of the symmetries of the material to symmetrize the susceptibility tensors. A degeneracy tolerance of 0.001 eV and a smearing width of 0.05 eV were used. The same smearing width was used in the VASP linear optical calculation to ensure proper benchmarking of dielectric function. Spin-orbit coupling was also taken into account, and the input parameters such as spin degeneracy and other parameters in both iNLO and VASP were adjusted accordingly.

CHAPTER III

MONOLAYER RESULTS

The structure, electronic properties, and nonlinear optical properties of monolayer Janus

MoSSe were investigated and are presented below.

Structure

The crystal structure of Janus 2D transition metal dichalcogenides (TMDCs) are

MXY, where M is a transition metal (e.g. Pd, Mo, W) and X and Y are chalcogenides (S, Se,

Te). Additionally, 2D TMDCs belong to hexagonal crystal systems with a three-fold rotation

axis (C_3), while some TMDCs have additional rotational axes. The structure can be seen in

Figure 2. Bond lengths and lattice parameters were found to be comparable to previous

literature.[49] The lattice constant is 3.25 Å, Mo-Se bond length is 2.53 Å, and Mo-S bond length is
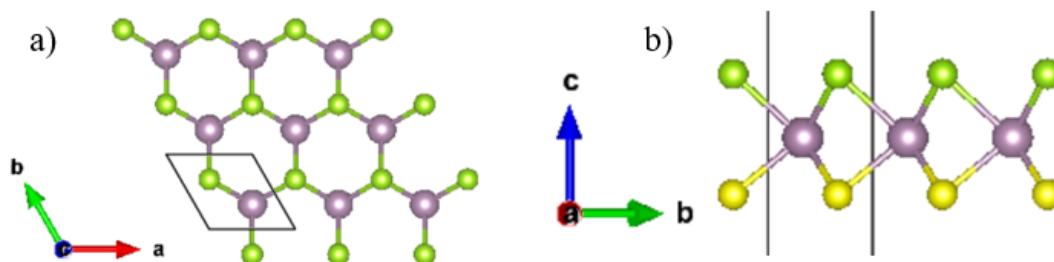
2.42 Å.

Figure 2: Janus monolayer MoSSe structure. a) c-axis view, and b) a-axis view. The purple
atoms are molybdenum (Mo), yellow atoms are sulfur (S), and green atoms are selenium (Se).

The monolayer structure exhibits C_{3v} symmetry, which includes a 3-fold rotation about

the c-axis, three vertical mirror planes, and it does not have inversion symmetry. Hence, it is

non-centrosymmetric. The lack of inversion symmetry is fundamental to the appearance of various physical properties. For example, piezoelectricity is a property that will be zero for any centrosymmetric material (or point group). Among the 32 crystallographic point groups for 3D systems, there are 11 point groups with inversion symmetry, and the other 21 do not have inversion symmetry. A full group theoretical analysis of this structure is subsequently performed.

Group Theoretical Analysis of NLO Properties

The NLO effects present in a material can be predicted using group theoretical analysis. An introduction to the group theoretical analysis of crystalline solids is provided in Supplementary Information. The SHG, shift current, and circular photocurrent effects are predicted using group theory as follows. The point group of Janus MoSSe is C_{3v}, and a character table is found in Table 4 in Supplementary Information.

The 2nd order susceptibility represents the coefficient of the 2nd term of the Taylor expansion of the polarization equation, seen below.

$$P_a = \chi^{(2)}_{abc} E_b E_c$$

P_a is the electric polarization along direction a induced by external field E_b and E_c. Both P and E are vectors and thus transform as $E + A_1$ in the C_{3v} point group. In order to obtain the representation of the desired property, the 2nd order susceptibility, we must take the direct product of the constituents, which are P_a, E_b, and E_c. The direct product of these representations give $\Gamma_P \otimes \Gamma_E = 2A_1 + A_2 + 3E$. This result gives the representations for the linear susceptibility $\chi^{(1)}_{ab}$, giving only two independent tensor elements since it has only two totally symmetric representations (A_1). Following Dresselhaus,[50] this product can and should be split into symmetric (Γ_s) and antisymmetric (Γ_a) portions that can be summed to produce $\Gamma = \Gamma_s + \Gamma_a$. The result is $\Gamma_s = 2A_1 + 2E$ and $\Gamma_a = A_2 + E$. Using the symmetric portion and discarding the

antisymmetric portion accounts for the permutation symmetry (PS). Now, a direct product of the symmetric portion a the second E-field will provide accurate SHG and shift current results with PS accounted for. The resulting direct product is $\Gamma_P \otimes \Gamma_{EE} = \Gamma_P \otimes \Gamma_E \otimes \Gamma_E = \Gamma_s \otimes \Gamma_E = 4A_1 + 2A_2 + 6E$. The four totally symmetric representations (A_1) necessitate four independent tensor elements in both SHG and shift current, since they both follow the 2nd order Taylor series expansion of polarization. Without accounting for PS, the result is $5A_1 + 4A_2 + 9E$. The overall process along with this result can be seen in Figure 3, though a further elaboration of the process is in Supplementary Information.
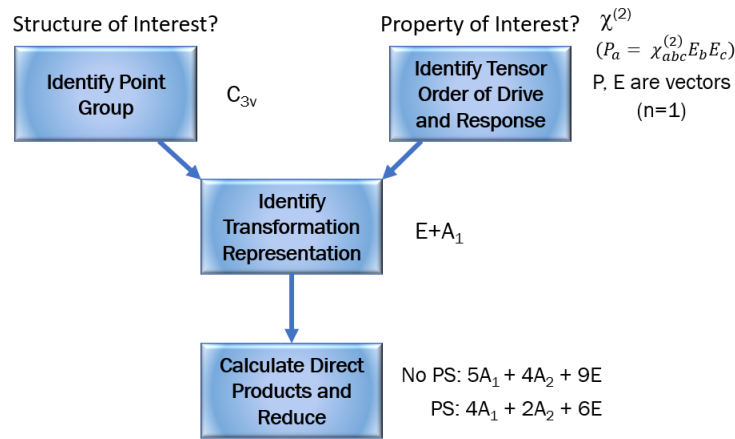
Figure 3: Example of C_{3v} analysis of 2nd order susceptibility

For circular photocurrent (CC), the driving force is incident light with circular polarization, which transforms as a R_i basis function, depending on incidence. Therefore, group theoretical analysis proceeds by doing all possible combinations of $i \otimes R_j$. Because z transforms as A_1, then there will not be any response in the z-direction due to circular photocurrent. This is necessarily the case because all direct products of R_i with an A_1, in this case, will not produce any A_1 representation, which is necessary for there to be a response. Additionally, $x \otimes R_z = y \otimes$

11

$R_z = E$, so there is no CC from these directions, either. The end result is four non-zero but non-independent tensor elements because $x \otimes R_x = x \otimes R_y = y \otimes R_x = y \otimes R_y = E^2$, which reduces to $A_1 + A_2 + E$. Therefore, group theory predicts one independent but four non-zero tensor elements for circular photocurrent in Janus MoSSe.

Electronic Structure

The electronic band structure was calculated for monolayer Janus MoSSe and is shown in Figure 4. The band gap was calculated to be 1.47 eV, and it is found to be a direct band gap with a K-K transition. The Fermi energy was set to the valence band maximum, which is located at K.
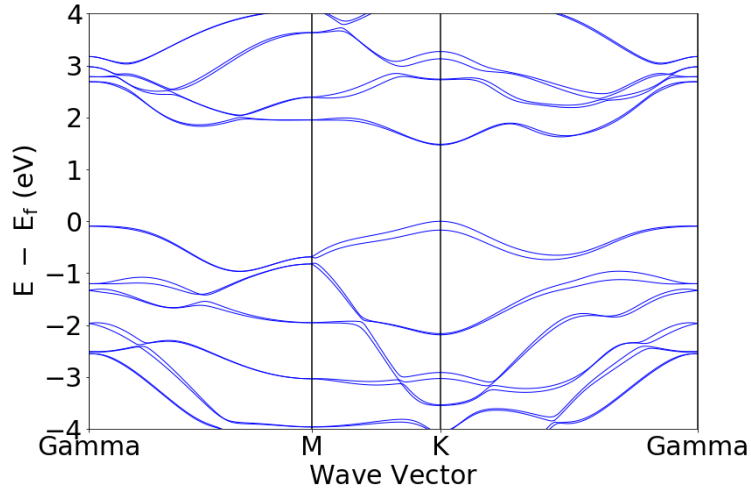

Figure 4: Electronic band structure of monolayer Janus MoSSe.

Nonlinear Optical Properties

The SHG susceptibility $\chi^{(2)}$, shift current susceptibility $\sigma^{(2)}$, and circular photocurrent (injection current) $\eta^{(2)}$ were calculated with SOC taken into account. The results are shown in Figure 5. The effect of SOC on the SHG can be seen in a later section.
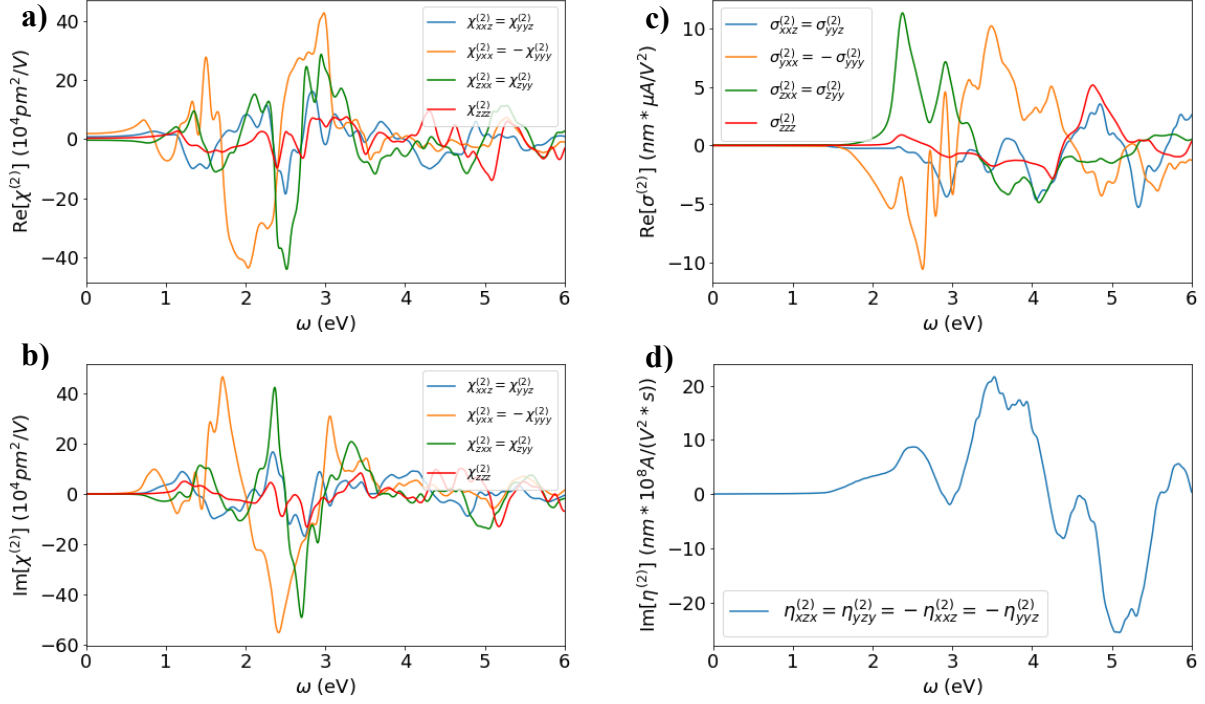
Figure 5: Nonlinear optical effects in Janus MoSSe monolayer. a, b) Real and imaginary part of second harmonic generation $\chi^{(2)}_{abc}$, respectively. c) Shift current $\sigma^{(2)}_{abc}$. d) Circular photocurrent $\eta^{(2)}_{abc}$. For a-c, only some of the element equalities are shown. The full equivalent tensor elements are: xxz=yyz=xzx=yzy, yxx=xxy=xyx= -yyy, and zxx=zyy. This is true of both SHG (a-b) and shift current (c). yxx= -yyy is the only antisymmetric relation. As shown in d), there is only one independent circular photocurrent susceptibility tensor element, which is in excellent agreement with the group theoretical analysis.

Figure 5a-b show the real and imaginary part of SHG, respectively, with a peak value along the yxx direction around $40 \times 10^4 pm^2/V$. This is comparable to MoS_2 and an order of magnitude greater than hexagonal boron nitride.[2] The significance of the result lies in the breaking of the horizontal symmetry in the Janus structure resulting in new directions of SHG and shift current (SC). Both SHG and SC are present and large in the out-of-plane direction, including zxx, zyy, and zzz. This opens up new applications in shift current based nonlinear photovoltaics[51] and other advanced optoelectronic applications.

There is an interesting result when inspecting the peaks of the shift current. Here, we chose the peak in the strong out-of-plane direction since that is most applicable in advanced optoelectronics and shift current photovoltaics.[51,52] From this peak, we extract the polarization anisotropy, which is remarkably similar at both peaks, as seen in Figure 6.
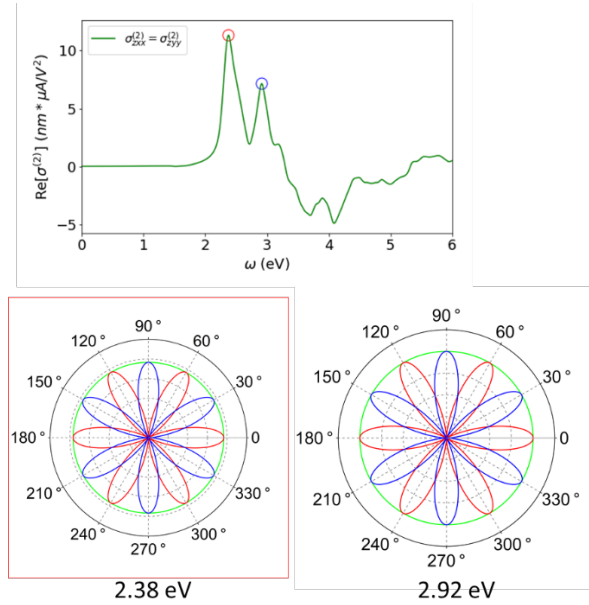
Figure 6: Shift current peaks and polarization anisotropy. The two peaks located at 2.38 eV and 2.92 eV show similar polarization anisotropy plots, with only slightly different maximum values.

Switching S and Se in the Janus structure reverses the chirality of the structure, which opens up a range of opportunities alongside some exciting recent results, such as evidence of gyrotropic order.[53] The result of the chiral structure can be seen in the out-of-plane shift current shown in Figure 7.

14
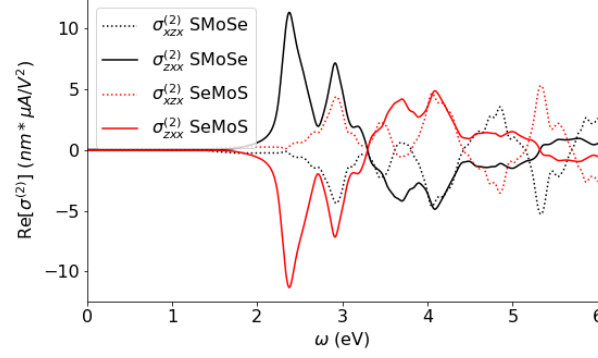
Figure 7: Result of switching S and Se on the out-of-plane shift current. Dotted-lines show shift current susceptibility tensor element $\sigma_{xzx}^{(2)}$, while the straight lines show $\sigma_{zxx}^{(2)}$. Black lines are for Janus SMoSe monolayer with the default configuration, while the red lines are for the switched structure, SeMoS. The result clearly demonstrates the current reversal upon S/Se switching in the Janus structure.

Next, the k-resolved NLO properties were calculated, including absorption, shift vector, and shift current. These k-resolved plots are essential for understanding the microscopic origin of the nonlinear optical properties of Janus MoSSe, and they are given in Figure 8. Close to the calculated bandgap (1.47 eV), absorption is exclusively at and around the high symmetry points in the Brillouin zone, namely K and K'. As the incident photon energy increases, the absorption in reciprocal space disperses out from the high symmetry k-points, but absorption is still minimal around the Γ-point. Figure 8d integrates the absorption over the photon energy to get an absorption cross-section approaching 20 $Å^2$. Figure 8e displays the shift vector, which approaches 10 Å around the high symmetry points, which is greater than the lattice parameter. For the shift vector, divergences caused by the optical zero-points were removed, and the cutoff used in our calculations was 25 Å. Finally, Figure 8f displays the k-resolved shift current for monolayer Janus MoSSe, which shows a very strong positive value around the high symmetry k-points and a strong negative value around the optical zero points. The result looks qualitatively similar to the shift vector.

15
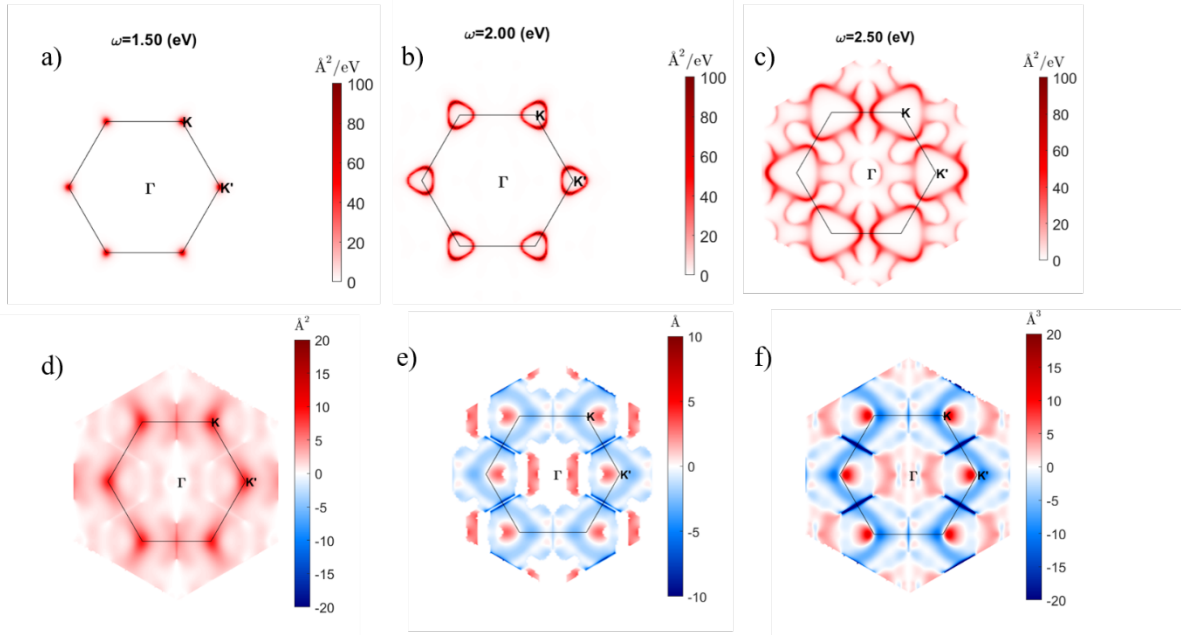
Figure 8: k-resolved NLO properties of monolayer Janus MoSSe. a-c) absorption at 1.5 eV, 2 eV, and 2.5 eV, respectively. d) Integrated absorption over all photon energies. e) shift vector with divergences removed f) shift current

Benchmarking Linear Optical Properties

In order to benchmark the used nonlinear optical code, iNLO, the linear optical properties were calculated and compared with those calculated by VASP. To ensure a proper comparison, the same smearing factor of 0.05 eV was used. The comparison shows great agreement as shown in Figure 9.
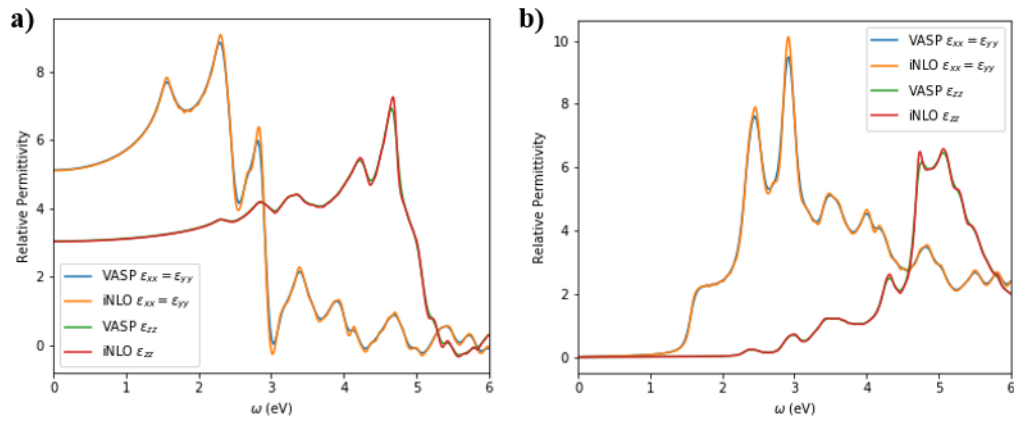
Figure 9: Comparison of dielectric function (or electrical permittivity) calculated by VASP and iNLO

Effect of Scissor Operator on Nonlinear Photocurrent

Because density functional theory usually underestimates the band gap of semiconductors, a bandgap correction is often applied. Hybrid functionals or GW calculations are two options to obtain a more accurate band gap. A simpler option is to apply a scissor operator that manually shifts band gap to a designated value as in most cases the band structures are often very similar except the main difference in the bandgap. In this case, we corrected the band gap to be about the average value of the experimental band gaps of MoS_2 and $MoSe_2$, since the properties are typically between their two values. In this case, the band gap was shifted from 1.47 eV to 1.75 eV. The effect of the scissor operator can be seen in Figure 10.
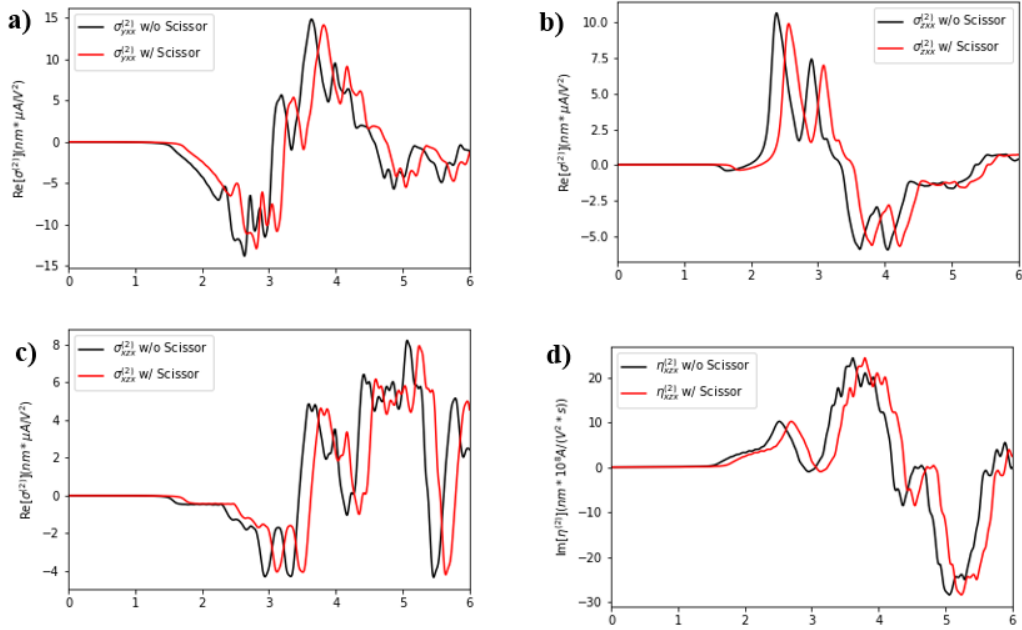
Figure 10: Effect of scissor operator on nonlinear photocurrent responses. a-c) three independent shift current tensor elements $\sigma_{yxx}^{(2)}$, $\sigma_{zxx}^{(2)}$, and $\sigma_{xzx}^{(2)}$. d) injection current tensor element $\eta_{xzx}^{(2)}$ (the only independent element).

The scissor operator shifts the entire curve by 0.28 eV to the right, while leaving the qualitative shape of the curve identical to the unshifted result. This is intuitive, since one can see little to no excitation below the band gap energy, and so this effect gets shifted to the right to correspond to the new band gap (1.75 eV) as an approximately average experimental value.

Effect of Spin-Orbit Coupling on SHG

Spin-orbit coupling (SOC) can have a large impact on the properties of materials such as , including optoelectronic properties. This coupling is larger for materials with heavy elements containing d- and f-electrons. Since molybdenum is a transition metal, it has d-orbitals with large orbital angular momentum and thus might have large spin-orbit coupling effects. Our results show that the SOC does have some effect on SHG, but not very large. The effect of SOC can be seen in Figure 11.
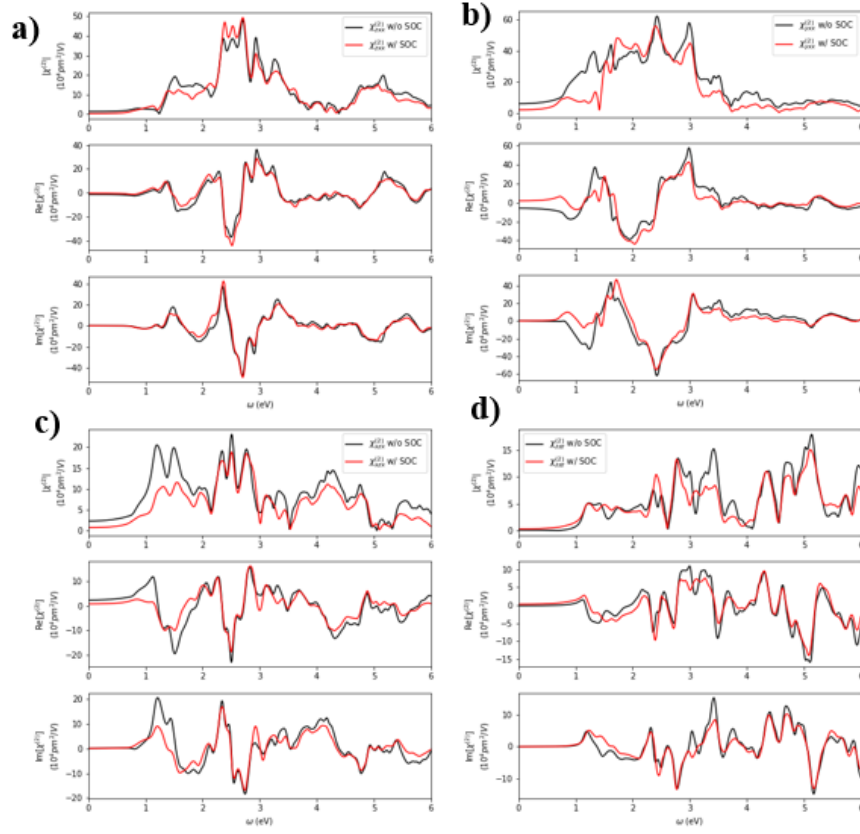
Figure 11: SHG with and without spin-orbit coupling for a) $\chi^{(2)}_{zxx}$, b) $\chi^{(2)}_{yxx}$, c) $\chi^{(2)}_{xzx}$,, and d) $\chi^{(2)}_{zzz}$, representing the four independent tensor elements of SHG susceptibility present in Janus MoSSe.

The SOC affects the SHG xzx tensor element $\chi^{(2)}_{xzx}$, and its magnitude is reduced by a factor of two in the region of 1-2 eV. It does not substantially affect the tensor elements along the out-of-plane direction. Figure 11a shows the $\chi^{(2)}_{zxx}$ SHG susceptibility tensor element, and it even shows a slight boost in the SHG when SOC is accounted for from 2-2.5 eV.

CHAPTER III

HETEROSTRUCTURE AND BILAYER RESULTS

Bilayer Stacking Configurations

There are five ways to stack MX_2 2D materials in a bilayer configuration, but different notations have been used in the literature. This section presents a summary of the different notations and recommends a path forward, and it will introduce the five different stacking configurations for our study.

Peng et al.[54] performed a stacking stability study with different bilayer configurations of MoS_2. The stacking structures were: AA, AB, AA', AB', and A'B, which can be grouped into those without inversion symmetry (type I): AA and AB, and those with inversion symmetry (type II): AA', AB', and A'B. Some inconsistency exists in their used notation compared to the references cited in their work. A summary of the differences in notation in the literature is given in Table 1.

Another group[55] claimed to follow notation previously introduced for h-BN stacking configurations.[56] The notation they used, however, disagrees with the h-BN study. Additionally, it is unintuitive because AB for them includes a rotation. Therefore, the notation of Peng and coworkers[54] is used in this work, which is identical to the h-BN study where AB is a translational shift from AA rather than including a rotational shift. Following the h-BN study, AA' is eclipsed stacking, which means they are overlapping but not completely like AA. AB is staggered, with atoms in the center of each hexagon. The transformation of an unprimed structure (AA or AB) to a primed structure (AA', A'B, or AB') requires rotation and cannot be obtained with translation only.[54,56] The transformation from AA to AB only requires translations.[54]

Table 1: Comparison of MoS_2 bilayer stacking configuration notations. The highlighted cells represent discrepancies from our notation, though AA and AA' are standard for all studies.

Reference	AA	AA'	AB	A'B	AB'
Peng (CPB 2014[54])	AA	AA'	AB	A'B	AB'
He (PRB 2014[55])	AA	AA'	AB'	A'B	AB
Liu (JPCC 2012[57])	AA	AA'	AB	AB'	A'B
Constantinescu (PRL 2013[56]) (h-BN)	AA	AA'	AB	A'B	AB'

Each stacking configuration has unique properties and can be determined visually in unique ways. Table 2 lists the characteristic features of the five stacking configurations, including their point group, space group, the presence/absence of inversion symmetry, atoms overlapping along the z-axis, and atoms present in the center of the hexagon, if any. Finally, the last row details how to transform one structure to another, with each structure being generated starting from AA configuration.

Table 2: Characteristic features of bilayer stacking configurations

	AA	AA'	AB	A'B	AB'
Point (Space) Group	D_{3h} (187)	D_{3d} (164)	C_{3v} (156)	D_{3d} (164)	D_{3d} (164)
Centrosymmetry	No	Yes	No	Yes	Yes
Overlapping Atoms	All	Mix	S-Mo	S-S (N-N)	Mo-Mo (B-B)
Center of hexagon	None	None	Mix	Mo (B)	S (N)
Transformations	$60°\rightarrow$AA' $(^1/_3,^2/_3)\rightarrow$AB	$(^2/_3,^1/_3)\rightarrow$A'B $(^1/_3,^2/_3)\rightarrow$AB'	-	-	-

These same five distinct stacking configurations of MX_2 are identical in the case of Janus MX_2, including Janus MoSSe. However, the Janus structure introduces different variations of each of these five configurations, such as reversing the atoms and thus the chirality (see monolayer results) of one or both of the layers. Other variations are chosen based on their experimental counterpart. True Janus bilayers can be produced using deterministic transfer techniques such as viscoelastic stamping,[58] while MX_2-Janus MX_2 heterostructures can be

produced using CVD. One option is to thermally selenize an MoS_2 bilayer, which replaces the top layer of sulfur with selenium.[49] Sulfurization of $MoSe_2$ has the opposite effect and replaces the top layer of selenium with sulfur.[29] We follow our experimental collaborators in using an MoS_2-SMoSe heterostructure, and the five unique stacking configurations for this heterostructure are shown in Figure 12.
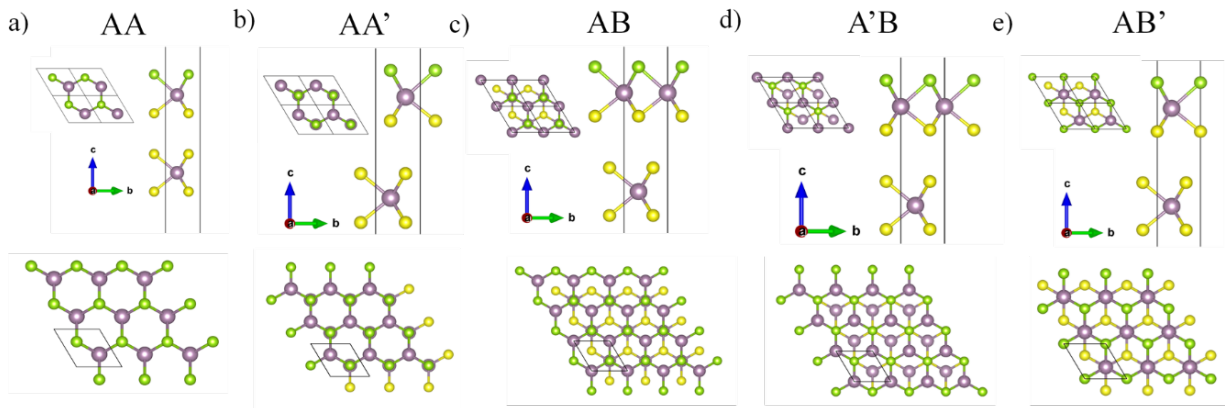
Figure 12: Stacking configurations of bilayer MoSSe. The bottom is the z(c-)axis, the middle is looking down the x(a-)axis, and the top left is a view of multiple unit cells to show the hexagonal structure. The purple atoms are molybdenum (Mo), yellow atoms are sulfur (S), and green atoms are selenium (Se).

Experimental Synthesis of Janus Heterostructures

Advancements in experimental techniques and interest in precise angles are approaching the ability to not only rapidly differentiate between stacking types, but also experimentally synthesize specific stacking types. Interest in precise angles is dominated from the magic angle of bilayer graphene,[59–63] though magic (twist) angles also play a role in other stacking materials (e.g. TMDCs) in generating Moiré superlattices.[64] One especially important advancement is precise rotational alignment[65] not only for superlattices but also for differentiating between the primed and unprimed stacking types. Other advancements include steps progressing

deterministic transfer,[66–68] inert environments beyond the standard glovebox,[69] and autonomous systems to find and/or stack crystal structures on substrates.[70,71] Continuing advancements will allow precise control over all possible stacking configurations in the experimental rather than just computational environment.

Nonlinear Optical Properties

The SHG susceptibility $\chi^{(2)}$ and shift current susceptibility $\sigma^{(2)}$ were calculated with SOC taken into account for each of the five bilayer stacking configurations of Janus MoSSe. The results for SHG and shift current susceptibilities for all five stacking configurations are given in Figure 13. The similarities and differences between SHG and shift current for a given stacking and direction are illuminating, as well as both SHG and shift current between different stacking configurations. AA and AB exhibit quite similar nonlinear optical response, while the unprimed configurations are different. A'B and AB' also exude similar response, indistinguishable at various incident photon energies. AA' is more similar to A'B and AB', but still not very closely. Finally, AB' seems to have smaller magnitude values in general. AB also has the strongest SHG of any of the configurations for its $\chi^{(2)}_{yxx}$.

Some of the main takeaways would be in the line of the application to optoelectronic devices, though interpreted with caution. For example, though AA has strong out-of-plane shift current, its application is limited because it is the highest energy configuration and thus most unstable. However, AB has very strong out-of-plane shift current and could be used in shift current photovoltaics or similar applications. Experimental advancements give hope to realization of applying particular stacking configurations to optoelectronic devices.
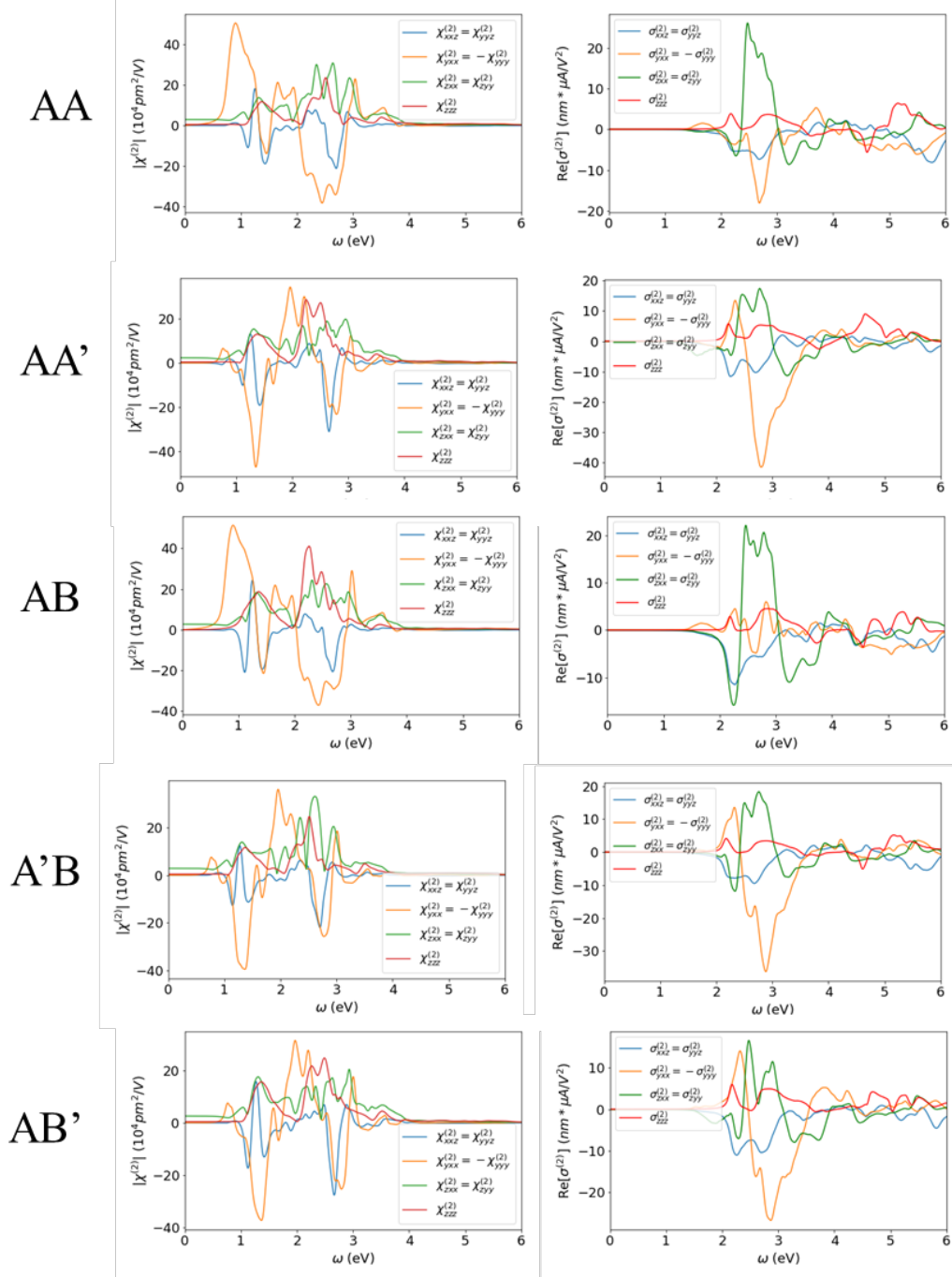
Figure 13: SHG magnitude (left column) and shift current (right column) of each of the five stacking configurations of the MoS$_2$-SMoSe heterostructure.

CHAPTER IV

CONCLUSION

Janus 2D materials are an exciting area of research due to their unique optoelectronic properties and applications. Here, we continue to expand a widely opening array of possibilities in the world of 2D materials and their heterostructures. Using VASP and an in-house developed code, we calculate the electronic, linear optical, and nonlinear optical properties of monolayer and bilayer Janus MoSSe. We demonstrate Janus MoSSe's feasibility as a shift current photovoltaic as a frequency doubler due to its high SHG and shift current, especially in the out-of-plane direction. The out-of-plane dipole is what enables these unique capabilities that are not possible in the non-Janus counterpart. The experimental demonstration of the bilayer Janus MX_2 materials still needs progress, but additional computational and experimental studies can explore different chiral structures of Janus MX_2 structures, and all possible combinatorial configurations of MX_2 materials in bilayer form, include MX_2-Janus MX_2 such as those discussed here.

REFERENCES

1. Novoselov, K. S. *et al.* Electric Field Effect in Atomically Thin Carbon Films. *Science.* **306**, 666–669 (2004).

2. Wang, H. & Qian, X. Giant optical second harmonic generation in two-dimensional multiferroics. *Nano Lett.* **17**, 5027–5034 (2017).

3. Maghirang, A. B. *et al.* Predicting two-dimensional topological phases in Janus materials by substitutional doping in transition metal dichalcogenide monolayers. *npj 2D Mater. Appl.* **3**, 35 (2019).

4. Chen, W., Hou, X., Shi, X. & Pan, H. Two-Dimensional Janus Transition Metal Oxides and Chalcogenides: Multifunctional Properties for Photocatalysts, Electronics, and Energy Conversion. *ACS Appl. Mater. Interfaces* **10**, 35289–35295 (2018).

5. Tang, X. *et al.* Distorted Janus Transition Metal Dichalcogenides: Stable Two-Dimensional Materials with Sizable Band Gap and Ultrahigh Carrier Mobility. *J. Phys. Chem. C* **122**, 19153–19160 (2018).

6. Zhang, F., Mi, W. & Wang, X. Spin-Dependent Electronic Structure and Magnetic Anisotropy of 2D Ferromagnetic Janus $Cr_2I_3X_3$ (X = Br, Cl) Monolayers. *Adv. Electron. Mater.* **6**, 1900778 (2019).

7. Li, F., Wei, W., Huang, B. & Dai, Y. Excited-State Properties of Janus Transition-Metal Dichalcogenides. *J. Phys. Chem. C* **124**, 1667–1673 (2019).

8. Zhang, Z., You, J.-Y., Gu, B. & Su, G. Strain-controlled magnetic and electric polarized states in two-dimensional magnetic Janus semiconductor. *arXiv Prepr. arXiv2001.02842* (2020).

9. Barhoumi, M., Lazaar, K., Bouzidi, S. & Said, M. A DFT study of Janus structure of S and Se in HfSSe layered as a promising candidate for electronic devices. *J. Mol. Graph. Model.* **96**, 107511 (2020).

10.   Zhou, W., Chen, J., Yang, Z., Liu, J. & Ouyang, F. Geometry and electronic structure of monolayer, bilayer, and multilayer Janus WSSe. *Phys. Rev. B* **99**, 075160 (2019).

11.   Zhou, W., Yang, Z., Li, A., Long, M. & Ouyang, F. Spin and valley splittings in Janus monolayer WSSe on a MnO(111) surface: Large effective Zeeman field and opening of a helical gap. *Phys. Rev. B* **101**, 45113 (2020).

12.   Ma, Y., Kou, L., Huang, B., Dai, Y. & Heine, T. Two-dimensional ferroelastic topological insulators in single-layer Janus transition metal dichalcogenides MSSe(M=Mo, W). *Phys. Rev. B* **98**, 085420 (2018).

13.   Yang, X., Singh, D., Xu, Z., Wang, Z. & Ahuja, R. An emerging Janus MoSeTe material for potential applications in optoelectronic devices. *J. Mater. Chem. C* **7**, 12312–12320 (2019).

14.   Yagmurcukardes, M., Sevik, C. & Peeters, F. M. Electronic, vibrational, elastic, and piezoelectric properties of monolayer Janus MoSTe phases: A first-principles study. *Phys. Rev. B* **100**, 045415 (2019).

15.   Bidmeshkipour, S. *et al.* Hydrogenated graphene oxide (H-G-SiO$_2$) Janus structure: experimental and computational study of strong piezo-electricity response. *J. Phys. D. Appl. Phys.* **53**, 175303 (2012).

16.   Ren, Y., Li, Q., Wan, W., Liu, Y. & Ge, Y. High-Temperature Ferromagnetic Semiconductors: Janus Monolayer Vanadium Trihalides. *arXiv Prepr. arXiv2001.02846* (2020).

17.   Kahraman, Z., Kandemir, A., Yagmurcukardes, M. & Sahin, H. Single-Layer Janus-Type Platinum Dichalcogenides and Their Heterostructures. *J. Phys. Chem. C* **123**, 4549–4557 (2019).

18.   Shi-Jun, L. & Kai-Lun, Y. Electronic and magnetic properties of the Janus MoSSe/WSSe superlattice nanoribbon: a first-principles study. *Phys. Chem. Chem. Phys.* **40**, 381–384 (2019).

19.   Liang, Y., Li, J., Jin, H., Huang, B. & Dai, Y. Photoexcitation Dynamics in Janus-MoSSe/WSe$_2$ Heterobilayers: Ab Initio Time-Domain Study. *J. Phys. Chem. Lett.* **9**,

2797–2802 (2018).

20.   Vo, D. D. *et al.* Band alignment and optical features in Janus-MoSeTe/X(OH)$_2$ (X = Ca, Mg) van der Waals heterostructures. *Phys. Chem. Chem. Phys.* **21**, 25849–25858 (2019).

21.   Pham, K. D. *et al.* First principles study of the electronic properties and Schottky barrier in vertically stacked graphene on the Janus MoSeS under electric field. *Comput. Mater. Sci.* **153**, 438–444 (2018).

22.   Yu, C., Cheng, X., Wang, C. & Wang, Z. Tuning the n-type contact of graphene on Janus MoSSe monolayer by strain and electric field. *Phys. E Low-Dimensional Syst. Nanostructures* **110**, 148–152 (2019).

23.   Li, Y. *et al.* Tunable interlayer coupling and Schottky barrier in graphene and Janus MoSSe heterostructures by applying an external field. *Phys. Chem. Chem. Phys.* **20**, 24109–24116 (2018).

24.   Deng, S., Li, L. & Rees, P. Graphene/MoXY Heterostructures Adjusted by Interlayer Distance, External Electric Field, and Strain for Tunable Devices. *ACS Appl. Nano Mater.* **2**, 3977–3988 (2019).

25.   Palsgaard, M., Gunst, T., Markussen, T., Thygesen, K. S. & Brandbyge, M. Stacked Janus Device Concepts: Abrupt pn-Junctions and Cross-Plane Channels. *Nano Lett.* **18**, 7275–7281 (2018).

26.   Li, X. *et al.* Two-dimensional Janus-In$_2$STe/InSe heterostructure with direct gap and staggered band alignment. *Appl. Surf. Sci.* **509**, 145317 (2020).

27.   Riis-Jensen, A. C., Deilmann, T., Olsen, T. & Thygesen, K. S. Classifying the Electronic and Optical Properties of Janus Monolayers. *ACS Nano* **13**, 13354–13364 (2019).

28.   Lu, A. Y. *et al.* Janus monolayers of transition metal dichalcogenides. *Nat. Nanotechnol.* **12**, 744–749 (2017).

29.   Zhang, J. *et al.* Janus Monolayer Transition-Metal Dichalcogenides. *ACS Nano* **11**, 8192–8198 (2017).

30.   Peng, R., Ma, Y., Zhang, S., Huang, B. & Dai, Y. Valley Polarization in Janus Single-Layer MoSSe via Magnetic Doping. *J. Phys. Chem. Lett.* **9**, 3612–3617 (2018).

31.   Ma, X., Wu, X., Wang, H. & Wang, Y. A Janus MoSSe monolayer: A potential wide solar-spectrum water-splitting photocatalyst with a low carrier recombination rate. *J. Mater. Chem. A* **6**, 2295–2301 (2018).

32.   Jin, C. *et al.* A Janus MoSSe monolayer: A superior and strain-sensitive gas sensing material. *J. Mater. Chem. A* **7**, 1099–1106 (2019).

33.   Thermoelectric properties of Janus MXY (M = Pd, Pt; X, Y = S, Se, Te) transition-metal dichalcogenide monolayers from first principles. *J. Appl. Phys.* **127**, 035101 (2020).

34.   Dong, L., Lou, J. & Shenoy, V. B. Large In-Plane and Vertical Piezoelectricity in Janus Transition Metal Dichalchogenides. *ACS Nano* **11**, 8242–8248 (2017).

35.   Idrees, M. *et al.* Optoelectronic and solar cell applications of Janus monolayers and their van der Waals heterostructures. *Phys. Chem. Chem. Phys.* **21**, 18612–18621 (2019).

36.   Long, C., Dai, Y., Gong, Z. R. & Jin, H. Robust type-II band alignment in Janus-MoSSe bilayer with extremely long carrier lifetime induced by the intrinsic electric field. *Phys. Rev. B* **99**, 115316 (2019).

37.   Materials, S. Band offsets engineering in asymmetric Janus bilayer transition-metal dichalcogenides. *J. Phys. Condens. Matter* 0–22 (2019).

38.   Guan, Z., Ni, S. & Hu, S. Tunable Electronic and Optical Properties of Monolayer and Multilayer Janus MoSSe as a Photocatalyst for Solar Water Splitting: A First-Principles Study. *J. Phys. Chem. C* **122**, 6209–6216 (2018).

39.   Yin, W. J., Wen, B., Nie, G. Z., Wei, X. L. & Liu, L. M. Tunable dipole and carrier mobility for a few layer Janus MoSSe structure. *J. Mater. Chem. C* **6**, 1693–1700 (2018).

40.   Hohenberg, P. & Kohn, W. Inhomogeneous electron gas. *Phys. Rev.* **136**, B864–B871

(1964).

41.   Kohn, W. & Sham, L. J. Self-Consistent Equations Including Exchange and Correlation Effects. *Phys. Rev.* **140**, A1133–A1138 (1965).

42.   Jain, A. *et al.* Commentary: The materials project: A materials genome approach to accelerating materials innovation. *APL Mater.* **1**, 011002 (2013).

43.   Kresse, G. & Furthmüller, J. Efficient iterative schemes for ab initio total-energy calculations using a plane-wave basis set. *Phys. Rev. B - Condens. Matter Mater. Phys.* **54**, 11169–11186 (1996).

44.   Kresse, G. & Furthmüller, J. Efficiency of ab-initio total energy calculations for metals and semiconductors using a plane-wave basis set. *Comput. Mater. Sci.* **6**, 15–50 (1996).

45.   Ong, S. P. *et al.* Python Materials Genomics (pymatgen): A robust, open-source python library for materials analysis. *Comput. Mater. Sci.* **68**, 314–319 (2013).

46.   Joubert, D. From ultrasoft pseudopotentials to the projector augmented-wave method. *Phys. Rev. B - Condens. Matter Mater. Phys.* **59**, 1758–1775 (1999).

47.   Blöchl, P. E. Projector augmented-wave method. *Phys. Rev. B* **50**, 17953–17979 (1994).

48.   Perdew, J. P., Burke, K. & Ernzerhof, M. Generalized gradient approximation made simple. *Phys. Rev. Lett.* **77**, 3865–3868 (1996).

49.   Lu, A. Y. *et al.* Janus monolayers of transition metal dichalcogenides. *Nat. Nanotechnol.* **12**, 744–749 (2017).

50.   Dresselhaus, M. S. *Applications of Group Theory to the Physics of Solids*. (2002).

51.   Cook, A. M., Fregoso, B. M., De Juan, F., Coh, S. & Moore, J. E. Design principles for shift current photovoltaics. *Nat. Commun.* **8**, 14176 (2017).

52. Chan, Y.-H., Qiu, D. Y., da Jornada, F. H. & Louie, S. G. Exciton Shift Currents: DC Conduction with Sub-bandgap Photo Excitations. *arXiv Prepr. arXiv1904.12813* (2019).

53. Xu, S. Y. *et al.* Spontaneous gyrotropic electronic order in a transition-metal dichalcogenide. *Nature* **578**, 545–549 (2020).

54. Tao, P., Guo, H. H., Yang, T. & Zhang, Z. D. Stacking stability of MoS_2 bilayer: An ab initio study. *Chinese Phys. B* **23**, 106801 (2014).

55. He, J., Hummer, K. & Franchini, C. Stacking effects on the electronic and optical properties of bilayer transition metal dichalcogenides MoS_2, $MoSe_2$, WS_2, and WSe_2. *Phys. Rev. B* **89**, 075409 (2014).

56. Constantinescu, G., Kuc, A. & Heine, T. Stacking in bulk and bilayer hexagonal boron nitride. *Phys. Rev. Lett.* **111**, 1–5 (2013).

57. Liu, Q. *et al.* Tuning electronic structure of bilayer MoS_2 by vertical electric field: A first-principles investigation. *J. Phys. Chem. C* **116**, 21556–21562 (2012).

58. Castellanos-Gomez, A. *et al.* Deterministic transfer of two-dimensional materials by all-dry viscoelastic stamping. *2D Mater.* **1**, 011002 (2014).

59. Song, Z. *et al.* All Magic Angles in Twisted Bilayer Graphene are Topological. *Phys. Rev. Lett.* **123**, 36401 (2019).

60. Tarnopolsky, G., Kruchkov, A. J. & Vishwanath, A. Origin of Magic Angles in Twisted Bilayer Graphene. *Phys. Rev. Lett.* **122**, 106405 (2019).

61. Cao, Y. *et al.* Unconventional superconductivity in magic-angle graphene superlattices. *Nature* **556**, 43–50 (2018).

62. Khalaf, E., Kruchkov, A. J., Tarnopolsky, G. & Vishwanath, A. Magic angle hierarchy in twisted graphene multilayers. *Phys. Rev. B* **100**, 85109 (2019).

63. Cheng, Y., Huang, C., Hong, H., Zhao, Z. & Liu, K. Emerging properties of two-

dimensional twisted bilayer materials. *Chinese Phys. B* **28**, 107304 (2019).

64. Sun, F. *et al.* Effects of magic angle on crystal and electronic structures of bilayer transition metal dichalcogenides. *arXiv Prepr. arXiv2003.09872.* (2020).

65. Kim, K. *et al.* Van der Waals Heterostructures with High Accuracy Rotational Alignment. *Nano Lett.* **16**, 1989–1995 (2016).

66. Frisenda, R. *et al.* Recent progress in the assembly of nanodevices and van der Waals heterostructures by deterministic placement of 2D materials. *Chem. Soc. Rev.* **47**, 53–68 (2018).

67. Zhao, Q., Wang, T., Ryu, Y. K., Frisenda, R. & Castellanos-Gomez, A. An inexpensive system for the deterministic transfer of 2D materials. *J. Phys. Mater.* **3**, 016001 (2020).

68. Taghavi, N. S. *et al.* Thickness determination of MoS2 , MoSe2, WS2 and WSe2 on transparent stamps used for deterministic transfer of 2D materials. *Nano Res.* **12**, 1691–1695 (2019).

69. Gant, P. *et al.* A system for the deterministic transfer of 2D materials under inert environmental conditions. *2D Mater.* (2020) doi:10.1088/2053-1583/ab72d6.

70. Masubuchi, S. *et al.* Deep-learning-based image segmentation integrated with optical microscopy for automatically searching for two-dimensional materials. *npj 2D Mater. Appl.* **4**, 4–6 (2020).

71. Masubuchi, S. *et al.* Autonomous robotic searching and assembly of two-dimensional crystals to build van der Waals superlattices. *Nat. Commun.* **9**, 4–6 (2018).

72. McMillan, J. A. Symmetry and Properties of Crystals: Theorem of Group Intersection. *Am. J. Phys.* **37**, 793–799 (1969).

73. Gelessus, A. Character tables for chemically important point groups. http://symmetry.jacobs-university.de/.

74.   Ashcroft, N. & Mermin, D. *Solid State Physics*. (Cengage Learning, 1976).

75.   Gelessus, A. Character table for point group C3v. http://symmetry.jacobs-university.de/cgi-bin/group.cgi?group=403&option=4.

SUPPLEMENTARY INFORMATION

Group Theoretical Analysis of Material Properties

Group theory is an essential tool in solid state physics to ascertain information about a material and its properties without requiring any experimentation or computation.[50] Here, I will provide a brief guide to solid-state group theoretical analysis with an example of linear susceptibility in Janus MoSSe. Knowledge of elementary introduction to group theory but not of its application to a full analysis in solid state physics, will be assumed, and I will be using Schoenflies notation. In order to apply group theory to analyze a material and its properties, one must know 1) its structure (point group symmetry), 2) the property of interest, and 3) the property's driving force and response (independent and dependent variable). Then, how the property and its associated variables transform in that point group has to be determined, which requires knowing the tensor order of the material property as well as its driving force and response. Once the transformation representation is found, then the direct product can be calculated and reduced using permutation symmetry to find the final sum of irreducible representations for that property. The total number of non-zero, independent tensor elements is ascertained from this final sum by the coefficient of the totally symmetric representation (e.g. A_1). The number of non-zero, independent tensor elements is the fundamental outcome of a group theoretical analysis that can be used to 1) predict material properties, 2) confirm experimental or computational results, or 3) simplify the required experimental measurements or theoretical calculations needed based on material symmetry. A schematic of this process is provided in Figure 14, with an elaboration subsequently provided.
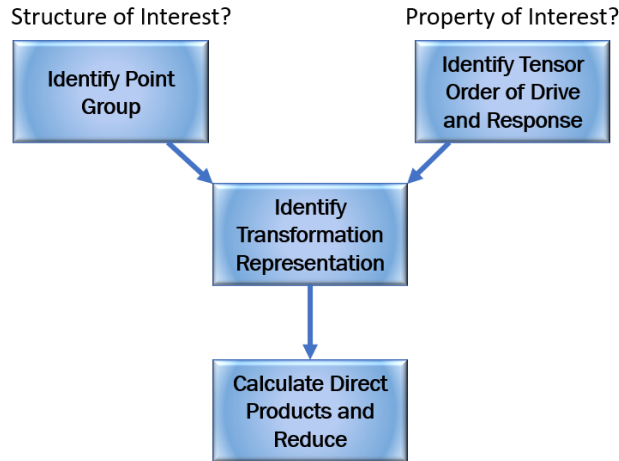
Figure 14: Typical process for group theoretical analysis

Material properties can be described with tensors, where a tensor of order n has n indices, or subscripts, which is also its number of dimensions. The order n designates how a property transforms within each point group based on the character table of that point group. Table 3 lists common material properties, driving forces, and response functions sorted by tensor order. The property of a material is what relates a driving force (independent variable) to the response function (dependent variable).[72] One important consequence of the tensor order is the basis functions that describe their transformation. Once the basis functions are known, then the transformation representation can be found by a character table by identifying the irreducible representation that corresponds to that basis function. Character tables can be found online[73] or in a reference book. For example, a driving force of tensor order 1 (a vector), such as electric field, will have linear basis functions. In the O_h point group, the electric field, along with any other vector, will transform as T_{1u} because all of the linear basis functions transform as T_{1u}. On the other hand, stress and strain, along with all tensors of order 2, will transform with the quadratic basis functions, indicating a transformation representation of $A_{1g} + E_g + T_{2g}$ in the O_h point group.

Table 3: Summary of material tensor properties, driving forces, and response functions with their basis functions. Conductivity, diffusion, and others are examples of linear susceptibilities. This table does not include pseudotensors, such as magnetic field. Pseudovectors require magnetic point groups to perform group theoretical analysis, which is neglected here.

Order of Tensor	Type	Response Function Examples	Material Property Examples	Driving Force Examples	Basis Functions
Zero	Scalar	Entropy (S)	Mass (m) Free Energy (F, G) Hall coefficient (R_H)	Temp. Diff. (ΔT)	None
One	Vector	Polarization (P_i) Displacement Field (D_i) Acceleration (a_i)	Young's Modulus (E_i)	Electric Field (E_i) Force (F_i)	Linear (x, y, z)
Two	Matrix	Strain (ε_{ij}), Stress (σ_{ij})	Linear Susceptibility ($\chi_{ij}^{(1)}$) Conductivity (σ_{ij}, k_{ij}) Permittivity (ε_{ij}) Shear Modulus (G_{ij}) Diffusion Coefficient (D_{ij}) Thermal expansion coeff. (α_{ij})	Stress (σ_{ij}), Strain (ε_{ij})	Quadratic (x^2, y^2, z^2, xy, xz, yz, yx, zx, zy)
Three	3D Array		Piezoelectricity (d_{ijk}) 2nd order susceptibility ($\chi_{ijk}^{(2)}$)		Cubic (x^3, xy^2, y^2z, etc.)
Four	4D Array		Elasticity (C_{ijkl}) 3rd order susceptibility ($\chi_{ijkl}^{(3)}$)		Fourth order (x^4, y^3z, xyz^2, x^2yz, xy^3, etc.)

The tensor order of the property can be found by adding the order (number of indices) of the driving force and the response.[72] It is worth noting that mass is listed as a scalar, which would be an exception to this principle; however, this may not strictly be the case. In special relativity, mass can be regarded a second order tensor. Additionally, in solid state physics, semiclassical substitutions in Newton's law from band theory result a second order "effective mass tensor."[74]

Example: Linear Susceptibility in Janus MoSSe

Now, I will do an example with linear susceptibility in the case of monolayer/bilayer Janus MoSSe, which are both in the C_{3v} point group. A character table for this point group can be found online[75] and is duplicated in Table 4.

Table 4: Character Table for the C_{3v} Point Group

C_{3v}	E	$2C_3$	$3\sigma_v$	Basis Functions
A_1	1	1	1	z
A_2	1	1	-1	R_z
E	2	-1	0	$(x,y)(R_x,R_y)$

The next step is to ascertain the tensor order of the driving force and response. As can be seen in the equation, $P_i = \chi_{ij}E_j$, both the driving force (external electric field) and response function (induced electric polarization) are vectors. Therefore, we must find the irreducible representations corresponding to the linear basis functions, since the constituents transform as vectors. For the C_{3v} point group, the irreducible representations are A_1 and E, as can be seen in the C_{3v} character table in Table 4. The vector representations for P and E are identical: $E + A_1$. Therefore, the "transformation representation" for each of the constituents can be considered as $E+A_1$. In order to obtain the representation of the desired property, the linear susceptibility χ_{ij}, we must take the direct product of the constituents, which are P_i and E_j. The direct product of these representations give $\Gamma_P \otimes \Gamma_E = 2A_1 + A_2 + 3E$. This result gives the representations for the linear susceptibility $\chi_{ab}^{(1)}$, giving only two independent tensor elements. One must further reduce the symmetry because of the permutation symmetry that exists, which requires splitting the resulting direct product into antisymmetric and symmetric representations.[50] The antisymmetric representations are found with the character table in the rows that have basis functions of R_i, since these are rotation matrices. In this case, the E representation contains both symmetric and antisymmetric components, so you can split representation in half for these.

The direct product of these representations gives $2A_1 + A_2 + 3E$. The basis functions for E are degenerate, which is required given the degeneracy of the E representation. Because the R_x

and R_y basis functions transform as E, but they are degenerate, one of the E representations are considered antisymmetric, and two are symmetric. Additionally, the A_2 is antisymmetric because of the R_z function in that column. Therefore, the representation breaks down into $\Gamma = \Gamma_s + \Gamma_a$, where $\Gamma_s = 2A_1 + 2E$ and $\Gamma_a = A_2 + E$. The result implies that the linear susceptibility only possesses two independent tensor elements because there are only two totally symmetric (A_1) representations from the resulting direct product.

Based on the information gained thus far, it is tempting to think one can skip the process of finding the direct products of constituents and merely find the correct basis functions corresponding to the tensor order of the material property (e.g. quadratic functions for $\chi_{ij}^{(1)}$ or ε_{ij}). One might think that since it is like multiplying two vector basis functions together that transform x or y, finding the quadratic basis functions like xy, x^2, etc. would give the correct answer. However, this gives an incorrect result. Even if one properly ignores the antisymmetric representations, this doesn't give you the correct number of each representation. At best, it can only give you one.